Monthly Notices
of the
ROYAL ASTRONOMICAL SOCIETY

MNRAS **475,** 1306–1322 (2018)
Advance Access publication 2017 December 13

doi:10.1093/mnras/stx3216

Characterization of polarimetric and total intensity behaviour of a complete sample of PACO radio sources in the radio bands

V. Galluzzi,[1,2★] M. Massardi,[1★] A. Bonaldi,[3] V. Casasola,[4] L. Gregorini,[1] T. Trombetti,[1,5,6] C. Burigana,[1,5,7] M. Bonato,[1] G. De Zotti,[8] R. Ricci,[1] J. Stevens,[9] R. D. Ekers,[9,10] L. Bonavera,[11] S. di Serego Alighieri,[4] E. Liuzzo,[1] M. López-Caniego,[12] R. Paladino,[1] L. Toffolatti,[11,13] M. Tucci[14] and J. R. Callingham[15]

Affiliations are listed at the end of the paper

Accepted 2017 November 30. Received 2017 November 14; in original form 2017 July 12

ABSTRACT

We present high sensitivity ($\sigma_P \simeq 0.6$ mJy) polarimetric observations in seven bands, from 2.1 to 38 GHz, of a complete sample of 104 compact extragalactic radio sources brighter than 200 mJy at 20 GHz. Polarization measurements in six bands, in the range 5.5–38 GHz, for 53 of these objects were reported by Galluzzi et al. We have added new measurements in the same six bands for another 51 sources and measurements at 2.1 GHz for the full sample of 104 sources. Also, the previous measurements at 18, 24, 33, and 38 GHz were re-calibrated using the updated model for the flux density absolute calibrator, PKS1934−638, not available for the earlier analysis. The observations, carried out with the Australia Telescope Compact Array, achieved a 90 per cent detection rate (at 5σ) in polarization. 89 of our sources have a counterpart in the 72–231 MHz GLEAM (GaLactic and Extragalactic All-sky Murchison Widefield Array) survey, providing an unparalleled spectral coverage of 2.7 decades of frequency for these sources. While the total intensity data from 5.5 to 38 GHz could be interpreted in terms of single component emission, a joint analysis of more extended total intensity spectra presented here, and of the polarization spectra, reveals that over 90 per cent of our sources show clear indications of at least two emission components. We interpret this as an evidence of recurrent activity. Our high sensitivity polarimetry has allowed a 5σ detection of the weak circular polarization for ∼38 per cent of the data set, and a deeper estimate of 20 GHz polarization source counts than has been possible so far.

Key words: galaxies: active – galaxies: statistics – radio continuum: galaxies.

1 INTRODUCTION

We have undertaken a long-term observational programme to characterize the spectra in total intensity and polarization of a complete sample of extragalactic radio sources over an unprecedented frequency range. The sources were drawn from the *Planck*–ATCA Coeval Observations (PACO) 'faint sample' (Bonavera et al. 2011), a complete sample flux-limited at $S_{20\,\mathrm{GHz}} \geq 200$ mJy, extracted from the Australia Telescope Compact Array (ATCA) survey at 20 GHz (AT20G; Murphy et al. 2010), and observed with the ATCA almost simultaneously with *Planck* observations. The PACO 'faint sample' is made up of 159 sources in the South Ecliptic Pole region where *Planck*'s scan circles intersect, providing maximal sensitivity.

In a previous paper (Galluzzi et al. 2017), we presented high sensitivity (rms errors $\sigma_P \simeq 0.6$ mJy; detection rate of about 91 per cent) multifrequency (six bands, from 5.5 to 38 GHz) polarimetry of a complete subsample of 53 compact extragalactic radio sources at ecliptic latitude $< -75^\circ$, observed in 2014 September.

In this work, we present new ATCA high sensitivity multifrequency polarimetric observations of a larger complete sample of 'PACO faint' sources, now comprising 104 objects. The frequency coverage was also extended adding polarimetric observations at 2.1 GHz. The broader frequency range has allowed a more comprehensive analysis of rotation measures (RMs). Moreover, our high sensitivity polarimetry has allowed a 5σ detection of the weak circular polarization for ∼38 per cent of data.

The observational determination of total intensity spectra was further extended exploiting the GLEAM (GaLactic and Extragalactic All-sky Murchison Widefield Array) survey data at 20 frequencies

★ E-mail: vincenzo.galluzzi@unibo.it (VG); massardi@ira.inaf.it (MM)

between 72 and 231 MHz (Hurley-Walker et al. 2017), available for 89 (≃86 per cent) of our sources.

The paper is organized as follows. In Section 2, we briefly present the observational campaigns. In Section 3, we describe the data reduction. In Section 4, we discuss the data analysis and the spectral behaviours in total intensity and polarization. In Section 5, we present source counts in polarization at ∼20 GHz, which is the selection frequency of our sample. Finally, in Section 6, we draw our conclusions.

2 OBSERVATIONS

The new observations were carried out in 2016 March and April, using the same array configuration (H214) and spectral set-up (three sets of 2 × 2 GHz CABB – Compact Array Broad-band Backend – bands centred at 5.5–9, 18–24, and 33–38 GHz) as in the previous campaign held in 2014 September, whose results are described by Galluzzi et al. (2017). The previous sample of 53 compact extragalactic sources is almost doubled (reaching a total of 104 sources) by adding the 'PACO faint' sources at ecliptic latitudes between −65° and −75°.

All the 51 additional sources were observed in the six CABB bands. Moreover, we re-observed all sources of the 2014 September sample at 5.5 and 9 GHz, while we managed to repeat the observations at 18–24 and 33–38 GHz only for 20 per cent of them. The whole sample of 104 objects was also observed at 2.1 GHz. We obtained three slots in three contiguous days to have the higher frequencies simultaneously observed. The total observing time was of ≃ 34 h, including overheads and calibration.

In order to achieve the same sensitivity level of previous observations (≃ 0.6 mJy), we integrated for 1 min at 2.1, 5.5, and 9 GHz, and for 1.5 min at the higher frequencies. The effective sensitivity reached in polarization at 2.1 GHz is a bit worse than requested, ≃ 1 mJy, due to significant radio-frequency interference (RFI). Weather conditions were good during the whole observing campaign. As done for the 2014 September observations, we considered only data from the five closest antennas in the H214 array configuration, discarding the baselines to the sixth and farthest antenna, since these are the most noisy. The synthesized beam size ranges from ≃ 90 to 5 arcsec in our frequency range.

3 DATA REDUCTION

Data were reduced via the MIRIAD software (Sault, Teuben & Wright 1995). Each frequency band was treated separately, as indicated in the ATCA User's Guide.[1] During the data loading, MIRIAD corrects for the time-dependent instrumental xy-phase variation, exploiting the known signal injected from a noise diode, which is mounted in one of the feeds of each antenna.

Our reference for the flux density absolute calibration (at all frequencies) is the source PKS1934−638, a gigahertz peaked-spectrum (GPS) radio galaxy: it is stable and unpolarized (at least below 30–40 GHz),[2] whose last model (see Sault 2003; Partridge et al. 2016) is now loaded into MIRIAD. This introduces a flux density difference with respect to the previous run, so we also re-calibrated the 2014 data. The new flux densities for the 20 GHz data are reported in this paper.

Once the calibration tables were derived, all solutions were ingested in the code for flux density extraction. As we did for the 2014 September observations, to better characterize the source spectra, we decided to split each 2 GHz-wide frequency band in subbands, except for the 2.1 GHz one that was kept unsplit because of the heavy RFI contamination. Each subband was calibrated separately. For total intensity, we split each band into 512 MHz-wide subbands. For polarized flux densities, we split bands in only two subbands to limit the $\Delta\nu^{-1/2}$ degradation in sensitivity.

Flux densities were estimated via the MIRIAD task UVFLUX. Our sources are known to exhibit linear polarization (up to ∼10 per cent; Massardi et al. 2008, 2013), defined by the Q and U Stokes parameters. Observations of the circular polarization of extragalactic radio sources have demonstrated that it is generally below 0.1−0.2 per cent, at least one order of magnitude lower than the linear polarization (Rayner, Norris & Sault 2000). Hence, the rms σ_V of the retrieved Stokes V parameter is frequently used as a noise estimator.

We achieved a 5σ detection of circular polarization, V, in ∼38 per cent of the data set, i.e. ∼89 per cent of the objects are detected in Stokes V in at least at one frequency.

Further discussion about the circular polarization is in Section 4.5. For only ∼15 per cent of detections, the circular to linear polarization ratio is ≥ 20 per cent; the mean circular polarization is substantially smaller than our calibration error of the polarized flux density, which is ≃10 per cent (Galluzzi et al. 2017). Since the contribution of Stokes V is so small, the polarized emission, P, can be estimated neglecting the V contribution and adopting σ_V as the rms noise for the Stokes parameters Q and U:

$$P = \sqrt{Q^2 + U^2 - \sigma_V^2}\,. \tag{1}$$

The σ_V^2 term removes the noise bias on P (e.g. Wardle & Kronberg 1974).[3] We find that ignoring the σ_V term in equation (1) results in a mean error of 0.01 per cent.

The polarization angle ϕ and fraction m (usually in terms of a percentage) are:

$$\phi = \frac{1}{2}\arctan\left(\frac{U}{Q}\right), \tag{2}$$

$$m = 100 \times P/I, \tag{3}$$

where the Stokes I is the total intensity flux density. The errors in total intensity, linear polarization flux density, and position angle were computed as in Galluzzi et al. (2017), i.e. adopting calibration errors of 2.5 per cent for I and of a conservative 10 per cent for the polarization fraction, P, for data between 5.5 and 38 GHz. At 2.1 GHz, due to the aforementioned RFI problems, we use a 5 per cent in I and a 12.5 per cent in P as calibration errors. Under the assumption of equal calibration errors for Q and U, Galluzzi et al. (2017) reported a ≃ 3° calibration error in the polarization position angle (3°.75 at 2.1 GHz). For circular polarization, we again assumed a 10 per cent (12.5 per cent at 2.1 GHz) calibration error (i.e. a factor ≃$\sqrt{2}$ larger than the calibration errors associated with Q and U). We note however that, due to the weakness of the signal and the corresponding lack of good calibrators, the calibration error for V is very difficult to estimate.

[1] www.narrabri.atnf.csiro.au/observing/users_guide

[2] It is the only known source with all these characteristics in the Southern sky.

[3] The error associated with the bias correction is negligible and will be ignored in the following.

4 DATA ANALYSIS

We adopt a 5σ level for detections in polarization. The median error is $\simeq 0.6$ mJy. We reach a detection rate of $\simeq$90 per cent for all the sources at all frequencies from 5.5 to 38 GHz. The number of detections is nearly uniform across the observed frequencies (99 sources detected at 5.5 GHz and 94 at 38 GHz). Following Galluzzi et al. (2017, their fig. 1), we checked the level of intraband depolarization in this frequency range, by subdividing each 2 GHz-wide band into 1 GHz-wide subbands. No systematic differences were found with respect to the previous assessment. At 2.1 GHz, due to the impact of RFI, we cannot proceed with this check, and the detection rate decreases to $\simeq$86 per cent. Three of our 107 observations include the extended source Pictor A. These observations were discarded for the following analysis that therefore deals with 104 compact objects.

4.1 Fit procedures

To fit the spectra, we used the same functional forms (a double power law and a triple power law) of Galluzzi et al. (2017), and adopted similar criteria about the minimum number of observations to properly constrain the fit parameters. Given the small fraction (less than 10 per cent) of non-detections, we do not use upper limits when performing the spectral fitting. About 85 per cent of the spectra could be successfully fitted in this way. In only three cases (AT20GJ041239-833521, AT20GJ054641-641522, and AT20GJ062524-602030), we do not have detections in polarization at enough frequencies to get a proper fit.

Similarly to what was found for the earlier sample, most (68 per cent) of our source spectra could be fitted with a double power-law down-turning at high frequencies. An upturning double power law was required in 15 cases, and a triple power law in 20 cases. The median values of the reduced χ^2 are 1.12 and 1.89 for Stokes I and P, respectively. The spectra for all the sources are presented in Fig. 1. The fitting curves and, when available, the previous PACO best epoch (2009–2010) observations in total intensity, and the AT20G best epoch (2004–2008) observations in total intensity and in polarization are also presented. In the lower part of each panel, we show the polarization fractions (both linear and circular, when detected), followed by the polarization position angles at the different frequencies.

4.2 Spectral properties of the sample

The spectral index $\alpha_{\nu_1}^{\nu_2}$ between the frequencies ν_1 and ν_2 is defined as

$$\alpha_{\nu_1}^{\nu_2} = \frac{\log\left(S(\nu_2)/S(\nu_1)\right)}{\log\left(\nu_2/\nu_1\right)}, \quad (4)$$

where $S(\nu_1)$ and $S(\nu_2)$ are the flux densities associated with the two frequencies. With respect to the previous work (Galluzzi et al. 2017), we simply add the 2.5 GHz to the reference frequencies 5.5, 10, 18, 28, and 38 GHz in order to preserve the equal spacing in logarithmic scale. Then, we proceed as usual for the spectral classification, taking into account $\alpha_{2.5}^{5.5}$ and α_{28}^{38} and again distinguishing in flat-(F), steep-(S), peaked-(Pe), inverted-(In), and upturning-spectrum (U) object.

We populate Table 1 with the outcome of the classification performed in total intensity and polarization, while we report the quartiles of distributions of spectral indices in Table 2. The basic conclusions of our analysis of the earlier, small sample are confirmed: less than 40 per cent of sources have the same spectral behaviour in total intensity and in polarization, and high- and low-frequency spectral indices are essentially uncorrelated, as shown in Fig. 2. The most populated entries of Table 1 are sources peaking both in total intensity and polarization and sources which are steep-spectrum in total intensity but have a spectral peak in polarization. This change in spectral shape towards a peaked- or even an upturning-spectrum in polarization might be the sign of Faraday depolarization which typically lowers the polarization signal at lower frequencies.

Galluzzi et al. (2017) pointed out that past high-frequency flux density measurements may suffer from the low accuracy of the model for the primary calibrator. In fact, they found that the mean high-frequency spectral index of 'PACO faint' sources in total intensity reported by Bonavera et al. (2011) was flatter by $\delta\alpha \sim 0.3$. In this work, we have taken into account the new model for the primary calibrator (PKS 1934−638) now encoded into MIRIAD. Since the model was not implemented yet, Galluzzi et al. (2017) applied a-posteriori corrections.

The differences with the results by Galluzzi et al. (2017) are relatively small. We confirm that the high-frequency spectral indices in total intensity and in polarization steepen at high frequencies and are essentially uncorrelated, although the mean values ($\alpha_{28}^{38} \simeq -0.75$ and $\alpha_{\rm P28}^{38} \simeq -0.80$, respectively) are less steep and closer to each other than found by Galluzzi et al. (2017). The distribution of sources among the different spectral types is also very similar; the biggest difference is in the fraction of objects classified as flat-spectrum in total intensity that increases from $\simeq$ 4 to $\simeq$21 per cent.

To extend the spectral coverage, we have exploited the information provided by the GLEAM survey at 20 frequencies between 72 and 231 MHz (Hurley-Walker et al. 2017). The spatial resolution is $\simeq$ 2 arcmin at 200 MHz, similar to the $\sim$90 arcsec resolution of our 2.1 GHz observations. We have 89 matching sources ($\simeq$86 per cent of our sample) in the GLEAM survey. For these sources, we have the unparalleled coverage of 2.7 decades in frequency. Since the GLEAM survey covers all the sky south of $+30^\circ$ in declination with a mean sensitivity of $\sim$10 mJy, and our sample is located between -86° and -42°, we can associate an upper limit of 50 mJy (at 5σ) to those sources without a GLEAM counterpart.

The fitting curves (triple power laws), although not always successful, generally show a good consistency between the ATCA and GLEAM measurements (cf. Fig. 3). But while in the range 5.5–38 GHz, the spectra are consistent with a single emitting region (Galluzzi et al. 2017), the GLEAM flux densities are clearly above the extrapolations from higher frequencies in $\sim$40 per cent of the cases, strongly suggesting the presence of at least another, generally steeper, component. The joint analysis with polarization data suggests even more complex structures (cf. Farnes, Gaensler & Carretti 2014, see Section 4.3).

4.3 Linear polarization fraction

Galluzzi et al. (2017) did not find any systematic variation of the mean polarization fraction with either flux density or frequency, down to $\simeq$ 5 GHz, in agreement with the results by Massardi et al. (2013). A similar conclusion was reached by Battye et al. (2011), who however had measurements only down to 8.4 GHz. On the other hand, claims of a systematic decrease of the polarization fraction with decreasing frequency were made by Agudo et al. (2010, 2014) and Sajina et al. (2011), suggesting that Faraday depolarization may work up to $\simeq$ 10 GHz or that the magnetic field is more ordered at high frequencies (Tucci et al. 2004). However, the conclusions by Agudo et al. (2010, 2014) and Sajina et al. (2011) may be

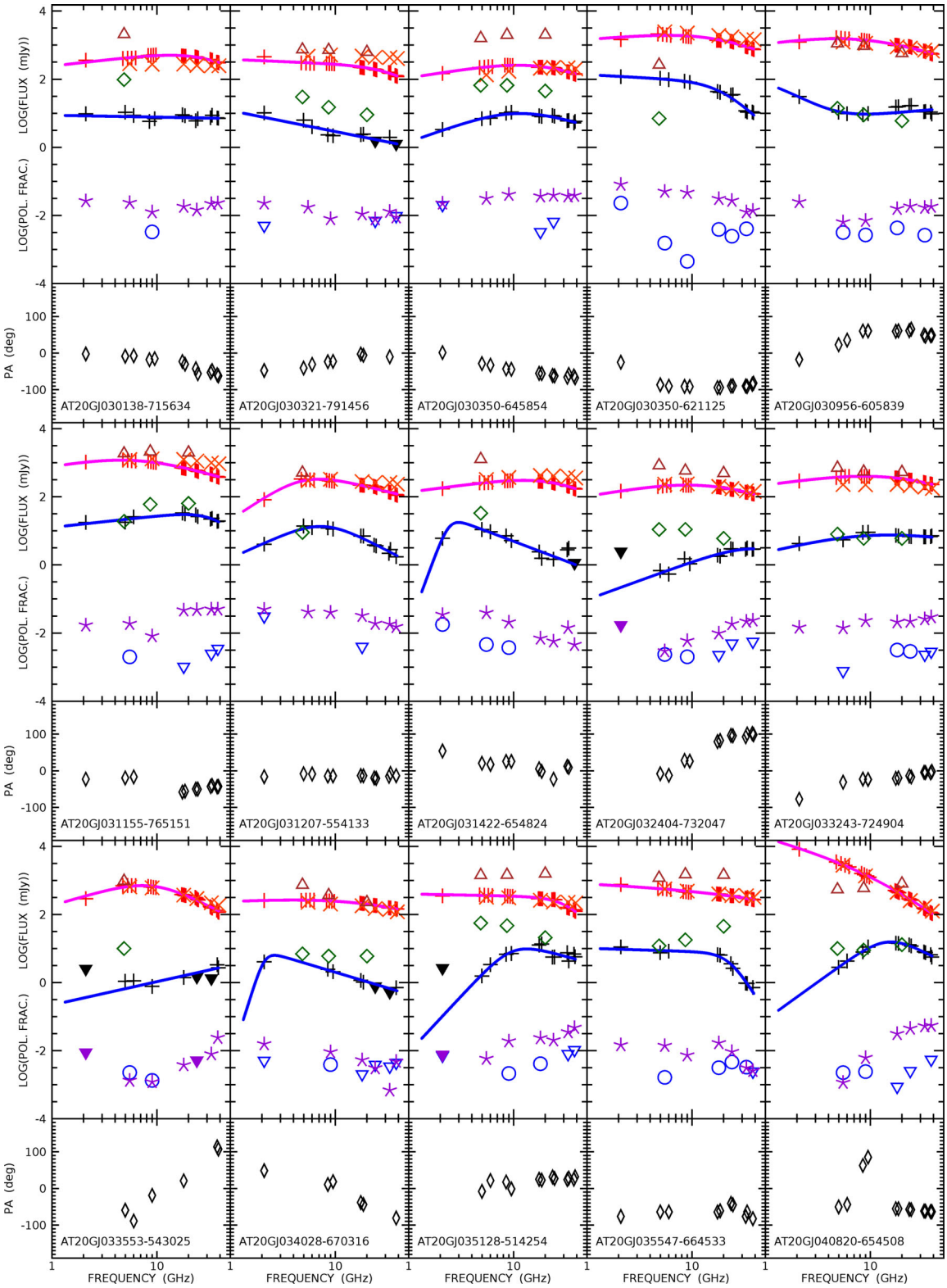

Figure 1. Spectra in total intensity and polarization, polarization fraction and polarization angle for the 107 objects of the faint PACO sample, observed in the 2014 September and 2016 March–April campaigns. The error bars are not displayed since they are smaller than the symbols. Total intensity: red pluses indicate our observations and the solid magenta lines show the fitting curves. The orange crosses show the median PACO flux densities (2009 July–2010 August) while the brown triangles represent the AT20G observations (best epoch in 2004–2008). Polarization (flux density): black pluses refer our observations. Upper limits are shown as black filled downwards triangles. The solid blue lines indicate the best-fitting curves. The AT20G observations (best epoch in 2004–2008) are represented by green diamonds. Other quantities available only for the 2014 September and 2016 March–April campaigns: linear polarization fractions: purple asterisks with upper limits shown as downwards pointing purple filled triangles; circular polarization fraction: violet circles and downward triangles for upper limits. Polarization angle (PA): black diamonds.

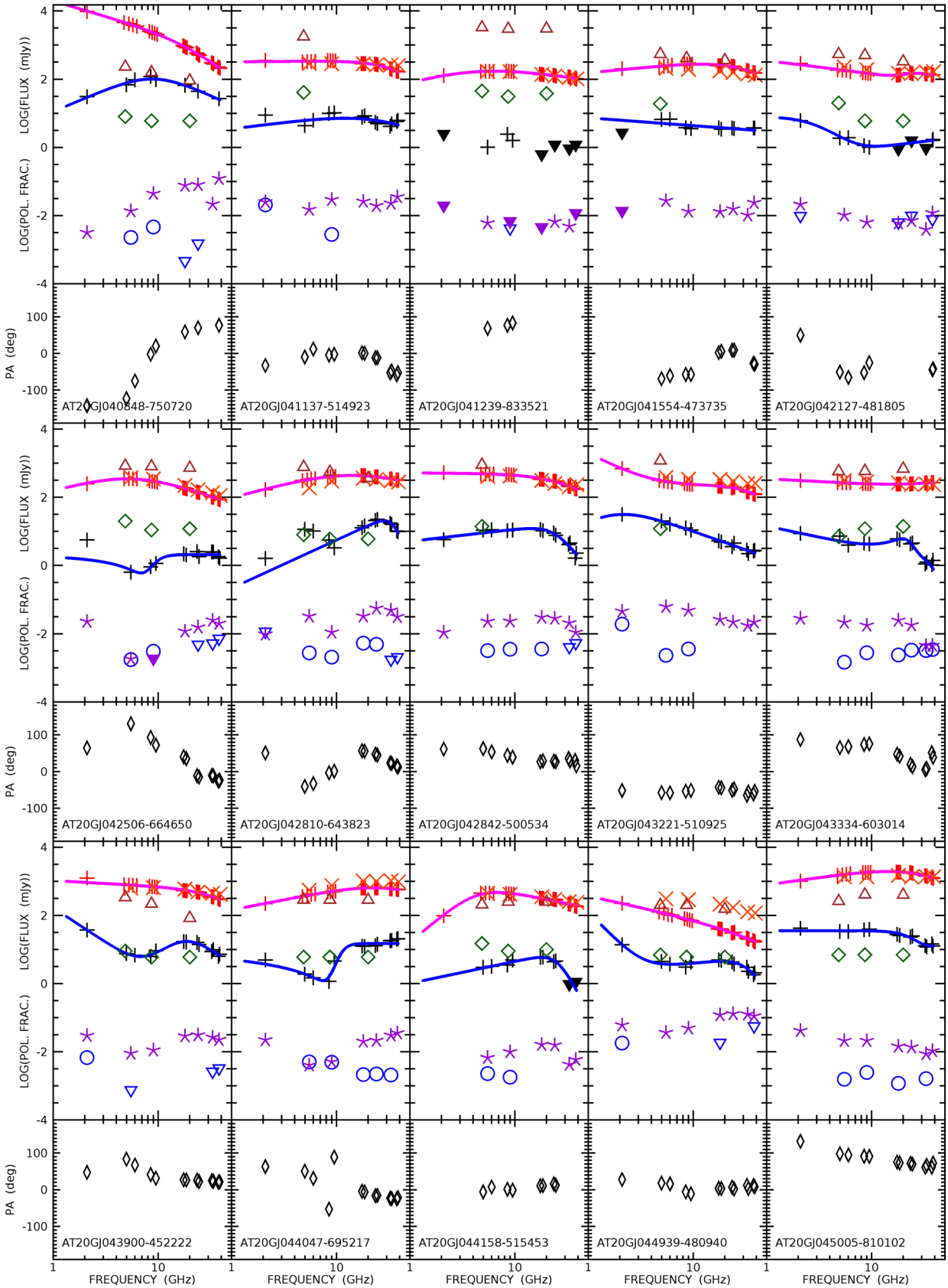

Figure 1 – *continued*

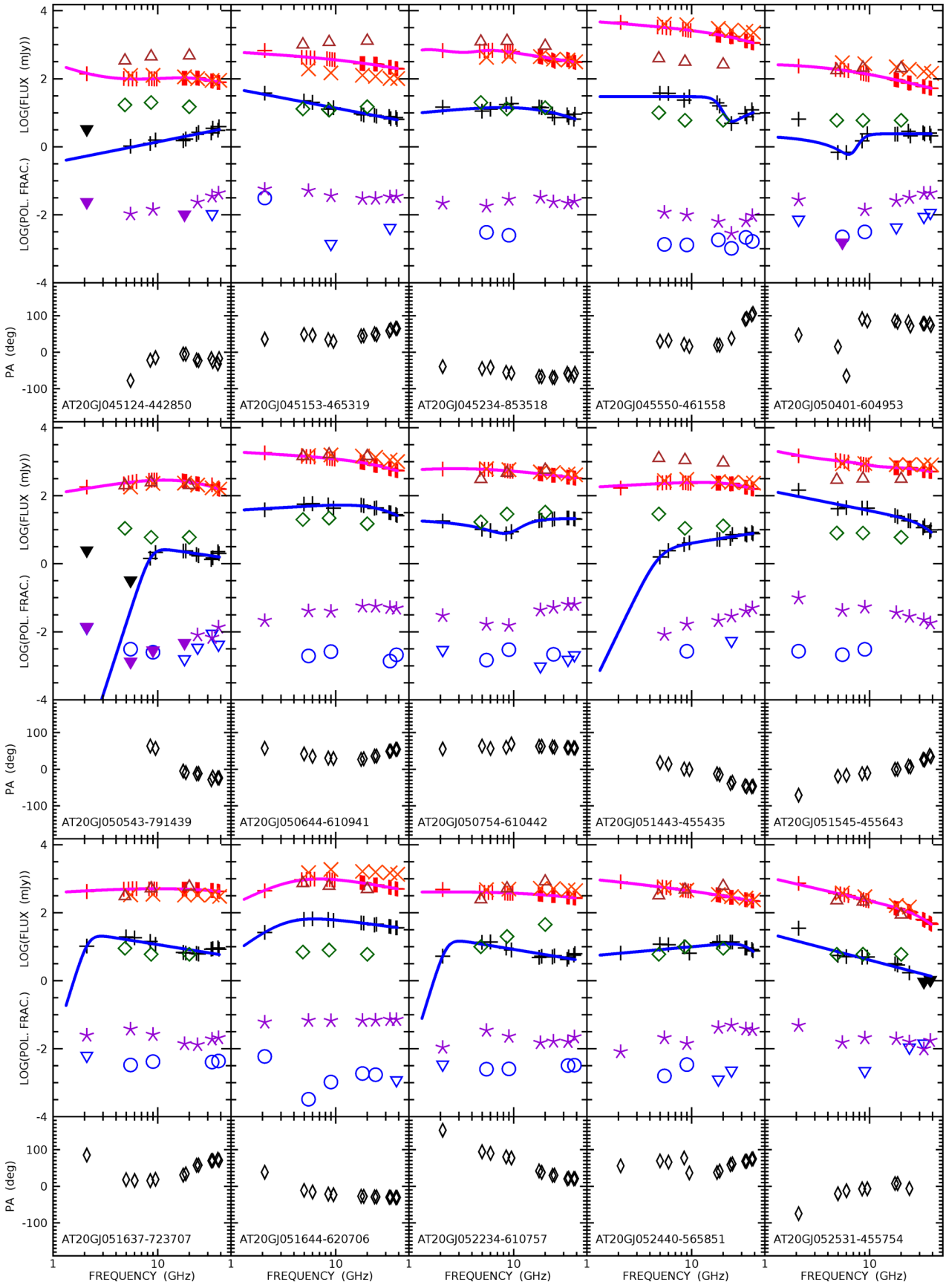

Figure 1 – *continued*

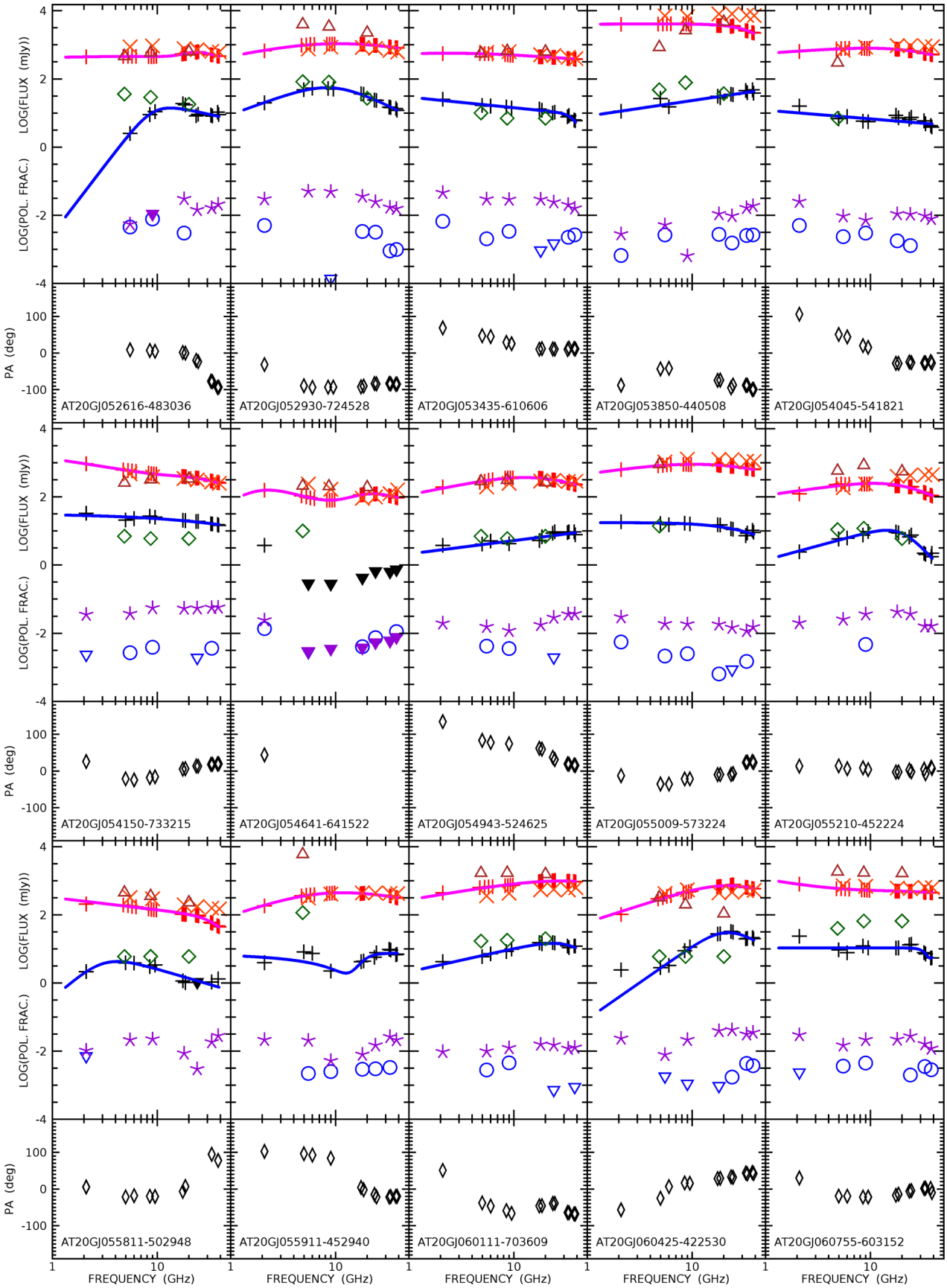

Figure 1 – *continued*

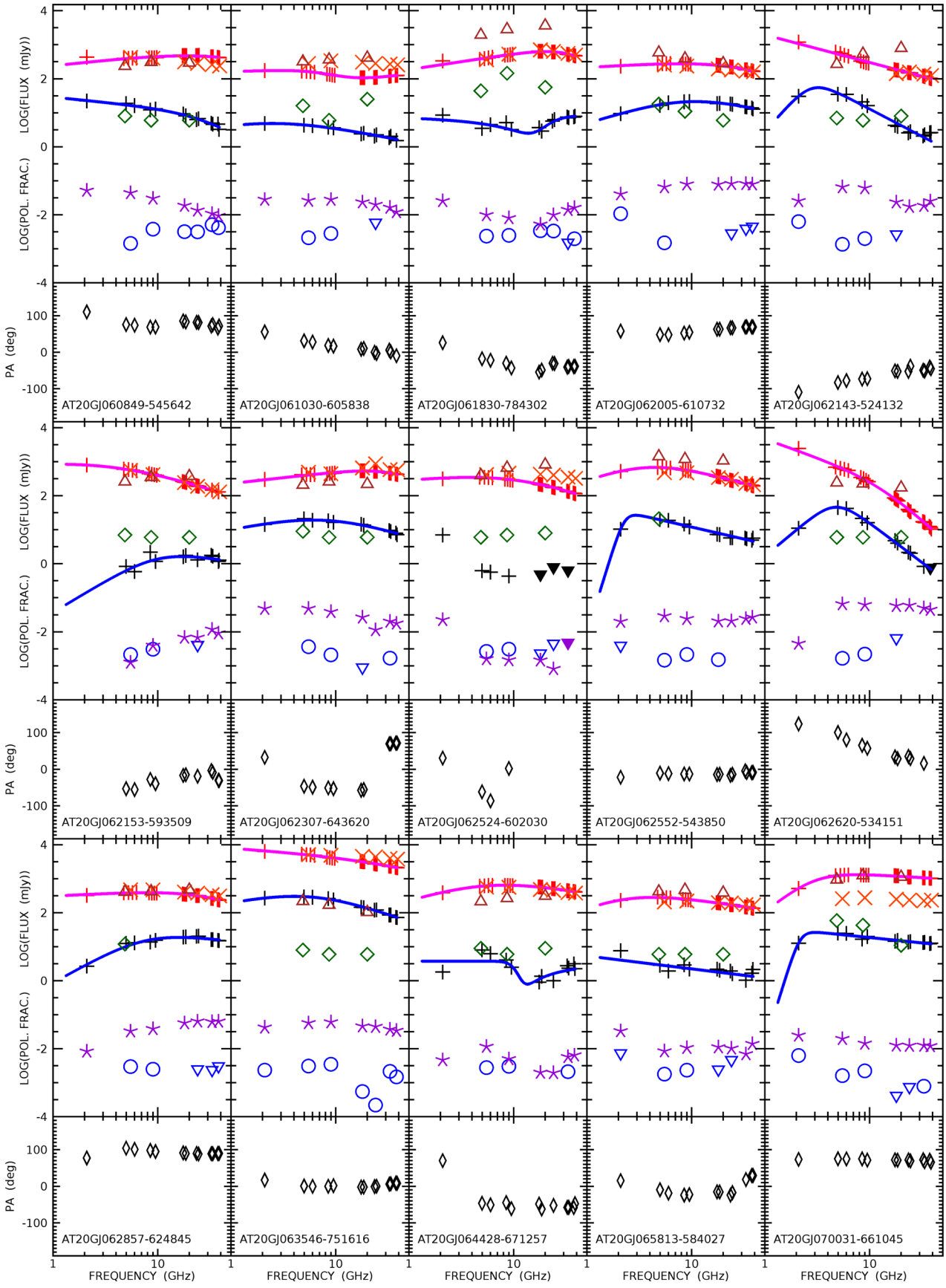

Figure 1 – *continued*

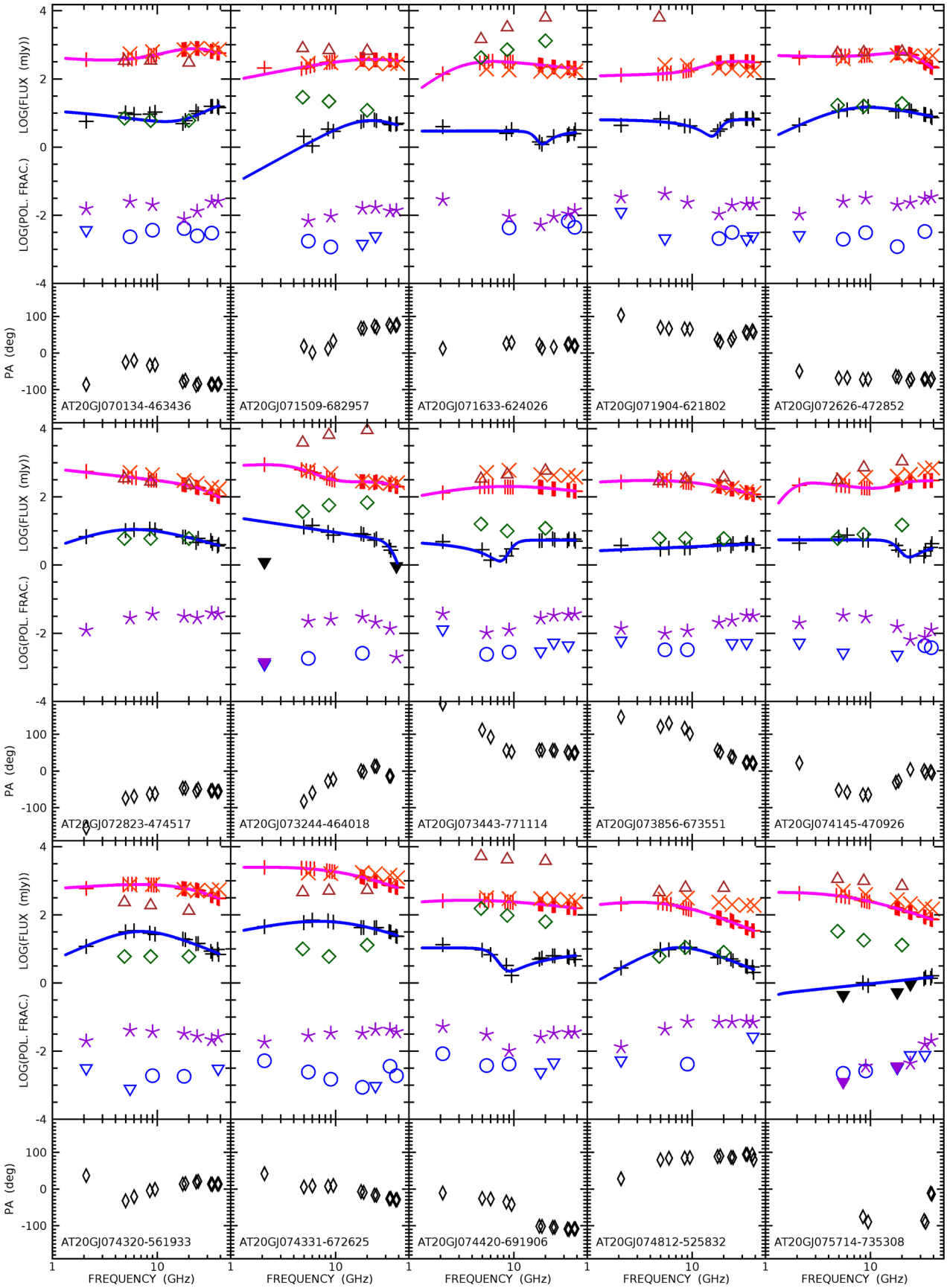

Figure 1 – *continued*

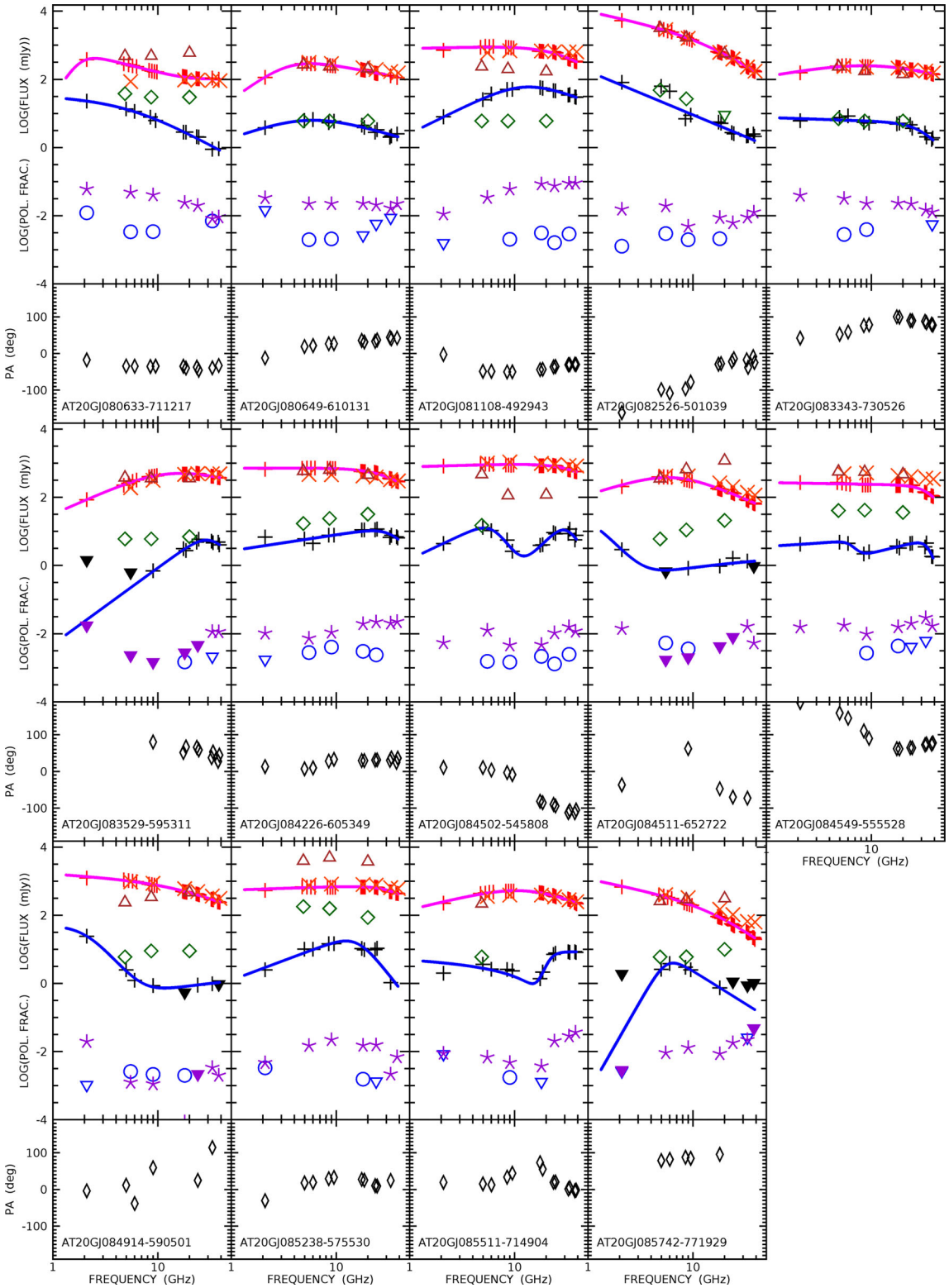

Figure 1 – *continued*

biased towards greater polarization fractions by not having taken into account non-detections (Tucci & Toffolatti 2012).

Our new observations allowed us to extend the spectra in polarized intensity down to 2 GHz and to have a factor of 2 larger sample. As for Galluzzi et al. (2017), our high detection rate (over 90 per cent) safeguards against any selection bias. Although the polarization fraction declines for several sources drops at lowest frequency (cf. Fig. 1), there is no statistical evidence of a decrease of the mean value for the whole sample or for its subsamples (cf. Table 3 and Fig. 4). However, as discussed below, such apparent uniformity may hide a more complex situation. The steep-spectrum objects (36) indeed show a slight trend, but comparing to the

Table 1. Distribution of sources per spectral type in total intensity and in polarization. The row 'NA' refers to the three objects classified in total intensity but missing a spectral fit in polarization. The last row reports the total for a given spectral class in total intensity, while the last column does the same in polarization.

Tot. Int. → Pol. Int. ↓	(In)	(Pe)	(F)	(S)	(U)	
(In)	0	3	0	1	0	4
(Pe)	0	24	4	20	0	48
(F)	0	5	4	4	0	13
(S)	0	5	8	7	0	20
(U)	0	8	5	3	0	16
(NA)	0	1	1	1	0	3
	0	46	22	36	0	

distributions of polarization fraction at 2.1 and 38 GHz, the rejection of the null hypothesis reaches the $\simeq 2\sigma$ level. The sample of flat-spectrum objects (22 objects in total) seems to reveal an opposite trend, but also in this case the significance is less than 3σ.

The spectra of the polarization fraction are less smooth than the total intensity spectra. Only about 15 per cent of the sources have an approximately constant polarization fraction over the full-frequency range. Five sources with smooth total intensity spectra above 2 GHz have double peaked fractional polarization, suggesting at least two emission components, seeing different screens. The polarization fraction of ∼15 per cent of the sources has an upturn at 2 GHz, where the emission components seen in the GLEAM data may yield a substantial contribution. The polarized flux from these components can drown out the decrease of the polarization fraction of the higher frequency component, due to Faraday depolarization. The most straightforward interpretation of these results is that the extension (and, correspondingly, the age) of emission components increases with decreasing frequency.

On the whole, a joint inspection of total intensity (including GLEAM measurements between 72 and 231 MHz) and polarization spectra indicates the presence of at least two (sometimes three) emission components for about 93 per cent of the sources. This is expected for GPS/CSS sources due to their double lobe structure (Tingay & de Kool 2003; Callingham et al. 2015). For about half of these, the clearest indication comes from polarization data. Hence, we reclassify our sample by distinguishing cases in which there is no sign of an additional synchrotron component (we label it '1C') from situations in which there are hints of two to three synchrotron components ('2–3C') or more complicated cases which seem to reveal more than three components in the spectrum. The latter are quite flat sources in total intensity from 70 MHz up to ∼30 GHz, where a steepening typically occurs. Among these 17 objects (≃16 per cent), 10 are classified in the flat (F) spectral category, i.e. objects with a flat spectrum in total intensity between 2.1 and 38 GHz.

According to Fig. 5, we do not have evidences of trends of the linear polarization fraction with the frequency for the full sample and for '1C' sources. '2–3C' sources have a minimum of the polarization fraction at ≃ 9 GHz, consistent with different emission components at lower and higher frequencies. For the >3C objects, whose spectra show indications of several overlapping synchrotron components, there is a hint of a *decrease* with increasing frequency (rather than of the increase expected by some authors, see e.g. Tucci & Toffolatti 2012) of the polarization fraction: the mean values decline from ≃2.1−2.4 per cent at ≤5.5 GHz to 1.2 per cent at 38 GHz. We anticipate here that in Section 4.4, we find these sources to have very large RMs at mm-wavelengths. This could indicate that their high-frequency components are characterized by a really dense and/or a magnetized medium that rotates the polarization angle strongly (cf. Pasetto et al. 2016).

Table 2. First, second (median), and third quartiles of spectral indices in total intensity and in polarization for different frequency ranges. We give values for the full sample and for the three main spectral classes, as classified in total intensity.

Tot. Int.		2.5–5.5			5.5–10			10–18 GHz	
Quart.	Q1	Q2	Q3	Q1	Q2	Q3	Q1	Q2	Q3
All	−0.29	−0.02	0.31	−0.35	−0.11	0.09	−0.46	−0.24	−0.08
Steep	−0.64	−0.33	−0.13	−0.67	−0.37	−0.22	−0.80	−0.46	−0.30
Peaked	0.10	0.32	0.54	−0.04	0.06	0.27	−0.30	−0.14	0.01
Flat	−0.16	−0.01	0.27	−0.25	−0.12	0.06	−0.26	−0.14	−0.05
Tot. Int.		18–28			28–38 GHz				
Quart.	Q1	Q2	Q3	Q1	Q2	Q3			
All	−0.75	−0.46	−0.27	−1.00	−0.75	−0.44			
Steep	−0.91	−0.76	−0.56	−1.56	−1.02	−0.81			
Peaked	−0.56	−0.42	−0.28	−0.85	−0.74	−0.56			
Flat	−0.33	−0.26	0.09	−0.42	−0.34	−0.20			
Pol. Int.		2.5–5.5			5.5–10			10–18 GHz	
Quart.	Q1	Q2	Q3	Q1	Q2	Q3	Q1	Q2	Q3
All	−0.28	0.15	0.85	−0.43	−0.06	0.38	−0.61	−0.15	0.34
Steep	−0.46	0.33	0.61	−0.59	−0.06	0.33	−0.74	−0.24	0.29
Peaked	−0.06	0.49	1.04	−0.19	−0.01	0.71	−0.35	−0.06	0.36
Flat	−0.57	−0.21	−0.06	−0.54	−0.29	−0.06	−0.59	−0.33	0.54
Pol. Int.		18–28			28–38 GHz				
Quart.	Q1	Q2	Q3	Q1	Q2	Q3			
All	−0.98	−0.53	0.02	−1.44	−0.80	−0.03			
Steep	−1.00	−0.76	−0.10	−1.47	−0.92	−0.37			
Peaked	−0.80	−0.32	0.31	−1.21	−0.73	−0.23			
Flat	−1.01	−0.54	0.14	−1.61	−0.68	0.04			

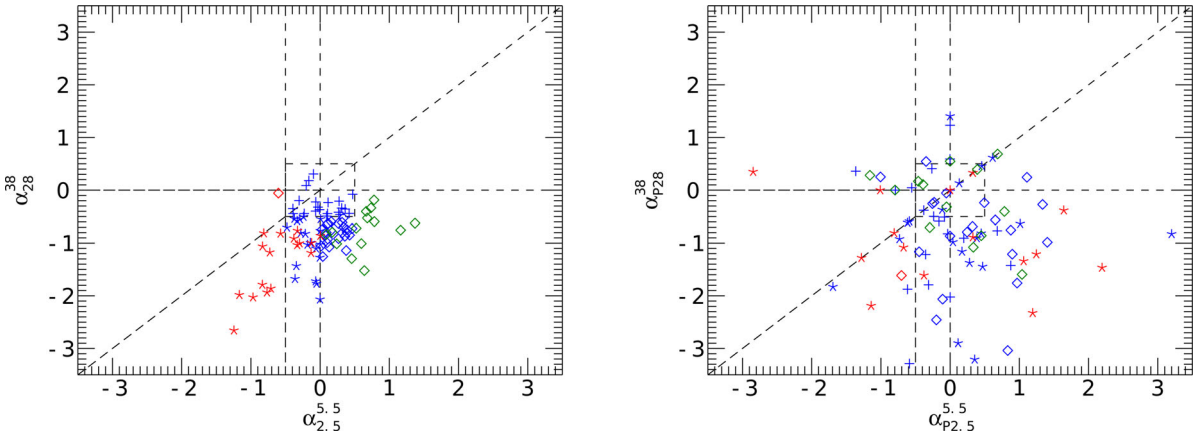

Figure 2. Radio colour–colour diagrams for (from left to right) total intensity and polarized flux density. Symbols identify the spectral type in total intensity: pluses for flat-spectrum, asterisks for steep-spectrum, diamonds for peaked-spectrum. Colours refer to the spectral shape between 2.5 and 18 GHz: red for steep-spectrum, blue for flat-spectrum, and green for peaked-spectrum sources.

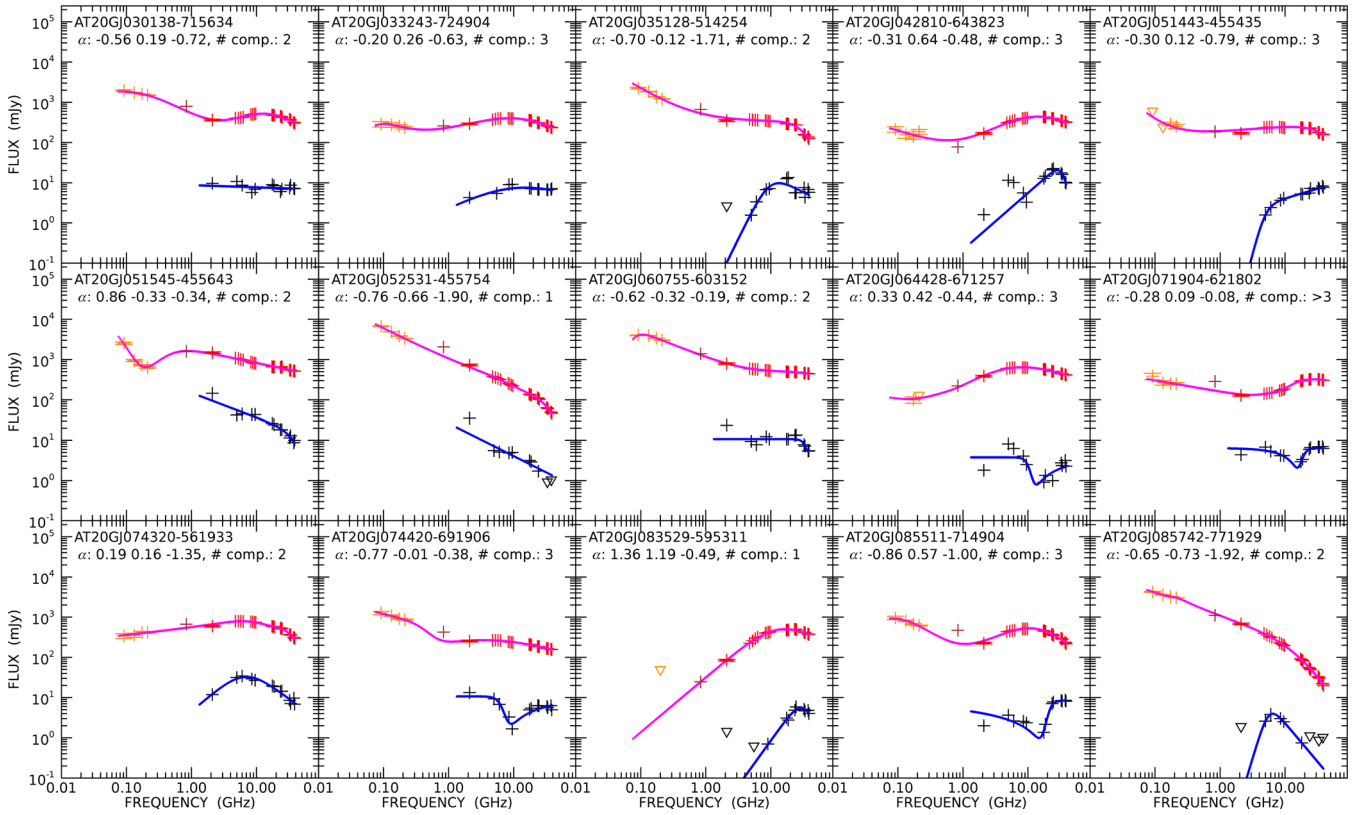

Figure 3. Spectra in total intensity and polarization taking into account GLEAM observations between 72 and 231 MHz (orange pluses). Our observations in total intensity are the red pluses, while black pluses and downward triangles (upper limits) are for polarization. The fits in total intensity and polarization are given as red and black solid curves, respectively. We report the SUMSS (Sydney University Molongo Sky Survey; Mauch et al. 2003) flux density at 843 MHz just for comparison, but we do not use it in the fit procedures. For each object, after its name, spectral indices (computed in total intensity) $\alpha_{0.2}^{0.4}$, $\alpha_{2.5}^{5.5}$, and α_{28}^{38} are provided. At the end of the title of each plot, there is the spectral classification in terms of estimated synchrotron components (see Section 4.3).

4.4 Polarization angle: cm- and mm-wavelength regime behaviour

The polarization angle was calibrated setting the parameter 'xycorr' in the MIRIAD task ATLOD which applies phase corrections provided by a noise diode mounted on one antenna feed. Partridge et al. (2016) found that the polarization angles measured by ATCA in this way agree with those measured by *Planck* based on the cosmic microwave background dipole measurements to within $\pm 2^{\circ}$.

Galluzzi et al. (2017) found evidence of non-zero Faraday rotation for only two objects (over a total of 53), since for the overwhelming majority of the sources the dependence of the RM with λ^2 has a complex behaviour. Only nine objects of our larger sample can be described by a linear RM–λ^2 relation over our full-frequency

Table 3. First, second (median), and third quartiles of the polarization fraction at each observed frequency given by the Kaplan–Meier estimator, taking into account the upper limits, for the full sample and for the steep- and peaked-spectrum sources. The last row reports probabilities for the null hypothesis (i.e. the two samples are drawn from the same parent distribution) given by the Kolmogorov–Smirnov test performed on the steep and peaked groups, considering together 5.5 and 9 GHz, the 18–38 GHz frequency interval and all the frequencies, respectively.

Class.	Frequencies (GHz)											
	2.1			5.5			9			18		
	Q1	Q2	Q3	Q1	Q2	Q3	Q1	Q2	Q3	Q1	Q2	Q3
All	1.09	2.16	2.98	0.84	1.88	3.25	0.79	1.65	3.02	0.99	2.01	3.07
Steep	0.95	1.54	2.54	0.81	1.74	3.23	0.95	1.64	3.69	0.87	2.33	3.13
Peaked	1.14	2.22	2.75	0.67	1.71	3.16	0.64	1.54	2.78	0.85	1.75	3.05
Flat	1.73	2.79	3.36	1.09	1.88	3.38	1.19	2.00	2.81	1.35	1.82	2.67
Prob.	(5.5–9 GHz)			0.825			(18–38 GHz)			8.176×10^{-4}		
Class.	Frequencies (GHz)											
	24			33			38					
	Q1	Q2	Q3	Q1	Q2	Q3	Q1	Q2	Q3			
All	1.06	1.95	2.87	1.17	1.85	3.29	1.20	2.09	3.54			
Steep	0.66	2.19	4.28	1.31	2.37	3.84	1.17	2.62	4.00			
Peaked	1.26	1.84	2.72	1.25	1.75	2.81	1.31	2.11	3.42			
Flat	0.98	1.64	2.45	0.66	1.60	2.08	1.06	1.40	2.11			
Prob.	(All freqs.)			0.011								

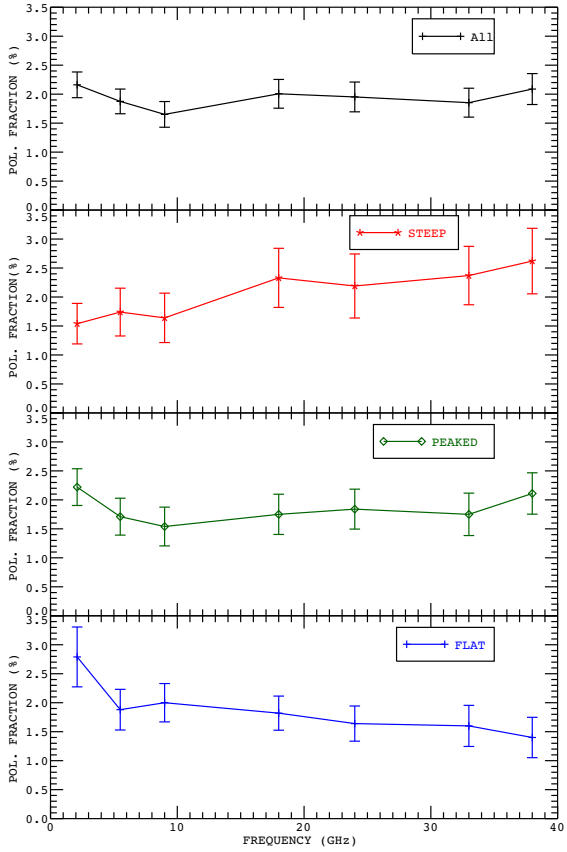

Figure 4. Median polarization fraction behaviour with frequency (at 2.1, 5.5, 9, 18, 24, 33, and 38 GHz) for all the sources (black), for steep sources (red), for peaked (green), and flat ones (blue). The errors on median values are given by $1.253 \times \mathrm{rms}/\sqrt{N}$, where rms is the standard deviation around the mean and N is the number of the data (at a given frequency) for a given class of objects (cf. Arkin & Colton 1970).

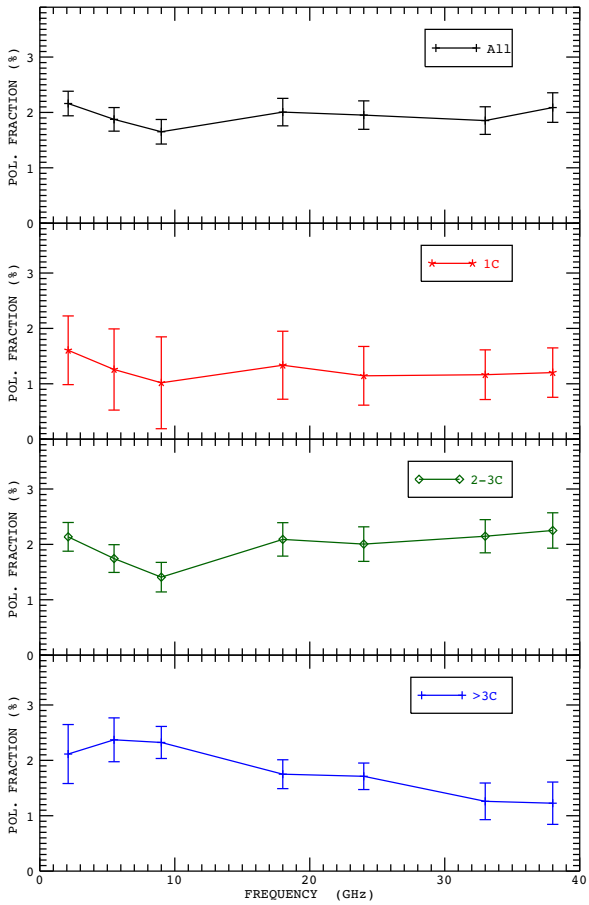

Figure 5. Median polarization fraction at the observation frequencies (2.1, 5.5, 9, 18, 24, 33, and 38 GHz) for all the sources (black), for '1C' sources (red), for '2–3C' sources (green), and for sources with more than three components (blue, labelled '>3C'). The errors on median values are given by $1.253 \times \mathrm{rms}/\sqrt{N}$, where rms is the standard deviation around the mean and N is the number of detected sources (cf. Arkin & Colton 1970).

Table 4. Median plus I and III quartile values of cm-wavelengths (upper table) and mm-wavelengths (lower table) RMs. In each table, the upper set of values refers to the observed RMs while the lower set refers to the RMs at the source for the subset of sources for which redshift measurements are available. In parenthesis are the numbers of sources in each group. Whenever the number of objects is <10, we provide only the median value. RMs are in rad m^{-2}.

All sample (42)				1C (3)			2–3C (31)			>3C (8)	
I	med	III	I	med	III	I	med	III	I	med	III
18	37	58	–	60	–	15	34	53	–	37	–
All sample (23)				1C (2)			2–3C (18)			>3C (3)	
I	med	III	I	med	III	I	med	III	I	med	III
40	94	244	–	335	–	46	84	220	–	122	–
All sample (59)				1C (4)			2–3C (50)			>3C (5)	
225	635	1397	–	342	–	283	637	1397	–	1141	–
All sample (27)				1C (2)			2–3C (22)			>3C (3)	
I	med	III	I	med	III	I	med	III	I	med	III
679	2300	5252	–	742	–	716	2351	5191	–	4022	–

range (2.1–38 GHz). For these sources, RM estimates are between −72 and 57 rad m^{-2}, with four cases compatible with a low (∼± 10 rad m^{-2}) or a null rotation.

Exploiting our larger frequency range, we can identify two regimes for the RM versus λ^2 relation, one at cm-wavelengths and the other at mm-wavelengths. We have investigated this more complex scenario by fitting the polarization angle as a function of the λ^2 separately for the two regimes (from 2.1 to 9 GHz and from 18 to 38 GHz). We required at least three measured polarization angles in each regime to perform the fit via the IDL 'linfit' procedure. A fit was regarded as acceptable when the reduced $\chi^2 < 2$ (probability >0.1). We obtained ∼40 and ∼57 per cent successful fits for the low- and high-frequency regimes, respectively. The corresponding median values of the reduced χ^2 are 0.37 and 0.69, respectively.

The medians and quartiles at cm- and mm-wavelengths are reported in Table 4 both for all objects for which acceptable fits were obtained and for the '1C', '2–3C', and '>3C' types, defined in Section 4.3. We warn the reader that the error associated with the estimated RMs can be large especially at the higher frequencies because of its dependence on $1/\lambda^2$. Typical uncertainties are of about 9 and 32 per cent at low and high frequencies, respectively; thus, while at the lower frequencies only two (∼5 per cent) of the estimated RMs are compatible with a null rotation at the 1σ significance level, this fraction raises to 15 per cent at the higher frequencies.

The median *observed* (i.e. uncorrected for the effect of redshift) values of the RM in the low-frequency regime are ∼40 rad m^{-2} irrespective of the spectral type. At high frequencies, they are larger for the whole sample (by a factor ∼15, i.e. ∼600 rad m^{-2}) and for '1C' or '2–3C' objects, and much larger for the >3C objects (∼1100 rad m^{-2}). Large values of RMs for multicomponent sources were previously reported by Pasetto et al. (2016), who suggested that the youngest, highest frequency components can be characterized by a really dense and/or a magnetized medium that strongly rotates the polarization angle.

So far, we dealt with *observed* RMs, $\mathrm{RM_{obs}}$. The RMs at the source, $\mathrm{RM_{AGN}}$, are related to $\mathrm{RM_{obs}}$ by Johnston-Hollitt & Ekers (2004):

$$\mathrm{RM_{obs}} = \frac{\mathrm{RM_{AGN}}}{(1+z)^2} + \mathrm{RM_{Gal}} + \mathrm{RM_{ion}}, \quad (5)$$

where $\mathrm{RM_{Gal}}$ and $\mathrm{RM_{ion}}$ are the contributions of our own Galaxy and of Earth's ionosphere, respectively. The Galactic contribution can typically vary from −300 to 300 rad m^{-2} depending on the line of sight. Our sample is located in a region around the Southern Ecliptic Pole and we adopt the Galactic Faraday rotation map provided by Oppermann (2014) to get the appropriate correction for each object of our sample. The ionospheric contribution is found to be typically $\lesssim$ 5 rad m^{-2} (Johnston-Hollitt & Ekers 2004) and can thus be safely neglected.

We have found redshifts in the AT20G catalogue (Mahony et al. 2011), and complemented them searching in the NED (NASA/IPAC Extragalactic Database) data base. For sources with redshift (44), we have also computed $\mathrm{RM_{AGN}}$ (see Table 4). The median low-frequency value is around 90 rad m^{-2}. At high frequencies, there seems to be a strong increase of the median $\mathrm{RM_{AGN}}$ from '1C' to '2–3C' to '>3C' objects (median $\mathrm{RM_{AGN}}$ of $\simeq$ 700, $\simeq$ 2400, and $\simeq$ 4000 rad m^{-2}), but the small number of '1C' and '>3C' objects prevents any firm conclusion. It is, however, remarkable that the large RMs of '>3C' objects echo the decrease of their median polarization fraction at mm-wavelengths (Section 4.3).

4.5 Circular polarization

The circularly polarized emission is weak, typically $\lesssim$0.1 per cent (Rayner et al. 2000), but potentially very interesting because its measurements may permit to gain information on various properties of jets, such as magnetic field strength and topology, the net magnetic flux carried by jets (and hence generated in the central engine), the energy spectrum of radiating particles, and the jet composition, i.e. whether jets are mainly composed of electron–positron pairs or electron–proton plasma (Ruszkowski & Begelman 2002).

The most obvious candidate for explaining circular polarization of compact radio sources is intrinsic emission, but the expected level under realistic conditions appears to be too low to explain the observed polarization (Wardle & Homan 2003). Pacholczyk (1973) pointed out that magnetic fields computed from the circular polarization, assuming that it is intrinsic, are usually so high as to cause a turnover in the intensity spectrum through synchrotron self-absorption at a considerably higher frequency than is actually observed. The most promising mechanism is Faraday conversion, a birefringence effect that converts linear to circular polarization (Ruszkowski & Begelman 2002; Wardle & Homan 2003).

At only two frequencies (5.5 and 9 GHz), more than 50 per cent of the sources were detected and thus median values of the circular polarization fractions, m_V, could be determined. We find

Table 5. Distribution of the polarization fractions at 18 GHz for the full sample.

Π (per cent)	Probability	Lower uncert.	Upper uncert.
0.600	0.2404	0.0453	0.0453
1.800	0.2644	0.0446	0.0446
3.000	0.1843	0.0381	0.0470
4.200	0.0721	0.0222	0.0317
5.400	0.0321	0.0153	0.0253
6.600	0.0160	0.0104	0.0211
7.800	0.0160	0.0104	0.0211
9.000	<0.018 43		
10.200	<0.008 01		
11.400	0.0080	0.0066	0.0184

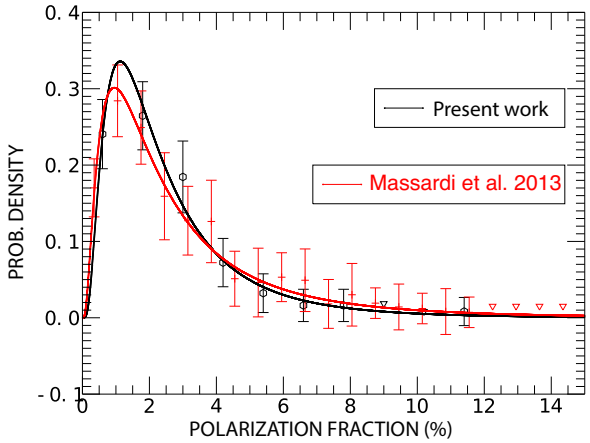

Figure 6. Distribution of the polarization fraction at 18 GHz. Errors and upper limits correspond to a 1σ level. The black circles refer to the sample studied in this paper, the red pluses to the full AT20G bright sample studied in Massardi et al. (2013). The corresponding fit by a lognormal distribution for each data set is reported with a solid lines of the same colour.

$m_{\rm V\,median} = (0.23 \pm 0.01)$ and (0.27 ± 0.02) per cent, respectively. For comparison, the median $m_{\rm V}$ for the Rayner et al. (2000) sample, selected at 4.85 GHz, estimated from the data in their table 3, is $\simeq(0.05 \pm 0.02)$ per cent. Our larger median values may be due to the fact that, because of the higher selection frequency, the overwhelming majority of objects in our sample are blazars; Rayner et al. (2000) have found that these objects have larger circular polarization fractions than radio galaxies that comprise a significant fraction ($\simeq$25 per cent) of their sample.

5 SOURCE COUNTS IN POLARIZATION

Fig. 7 shows the source counts in polarization at 20 GHz obtained through the convolution of the total intensity differential source counts reported by the model of De Zotti et al. (2005) with our distribution of polarization fractions at 18 GHz. In Table 5 and Fig. 6, we report the observed distribution (black circles): in each bin, uncertainties are derived assuming Poisson statistics, following the indications of Gehrels (1986). The solid line is the fit assuming a lognormal distribution

$$f(\Pi) = \text{const} \cdot \frac{1}{\sqrt{2\pi}\sigma\,\Pi} \exp^{-1/2 ln(\Pi/\Pi_{\rm m})^2/\sigma^2}, \quad (6)$$

Table 6. Euclidean normalized differential source counts at 20 GHz in polarization obtained in this paper via the convolution of the distribution of the polarization fraction at 18 GHz with the De Zotti model (2005).

log [$P(Jy)$]	$S^{5/2}n(S)$ (Jy$^{3/2}$sr^{-1})	Lower uncert.	Upper uncert.
−2.897	0.0667	0.0007	0.0007
−2.692	0.0760	0.0011	0.0011
−2.486	0.0869	0.0017	0.0017
−2.281	0.1011	0.0025	0.0025
−2.075	0.1198	0.0039	0.0039
−1.870	0.1426	0.0061	0.0061
−1.664	0.1662	0.0094	0.0094
−1.459	0.1856	0.0142	0.0142
−1.253	0.1978	0.0209	0.0209
−1.048	0.1987	0.0299	0.0299
−0.842	0.1886	0.0417	0.0519
−0.637	0.1734	0.0549	0.0766
−0.431	0.1580	0.0726	0.1199
−0.226	0.1447	0.0996	0.2034
−0.020	0.1337	0.1297	0.3606
0.185	<0.318 86		
0.391	<0.648 41		
0.596	<1.318 55		

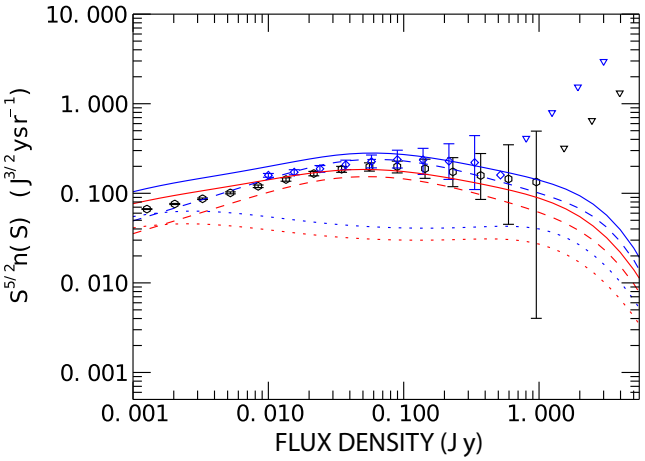

Figure 7. Differential source counts at 20 GHz in polarization obtained in this paper plotted with black circles (black downward triangles are for upper limits). Also shown, for comparison, are the estimates by Massardi et al. (2013) using the polarimetric data from their own survey, somewhat shallower than the present one ($S_{20\,\rm GHz} > 500$ mJy) combined with the full AT20G catalogue (blue diamonds and blue downward triangles for upper limits). The curves show the predictions of the Tucci & Toffolatti (2012) model: blue curves for the 'conservative' case and red curves for the 'optimistic' case. The solid lines represent the total number counts; the dotted lines are for steep-spectrum sources (classified at low frequencies); the dashed lines are for flat objects (flat-spectrum radio quasars, i.e. FSRQs and BL Lacs).

where const=0.96, $\sigma = 0.76$, and $\Pi_{\rm m} = 2.00$, i.e. the median value of the distribution. The reduced χ^2 value is 0.21. In Table 6 and Fig. 7 (black circles), we plot the differential source counts in polarization, following the recipe reported by Tucci & Toffolatti (2012): since there is no evidence of a correlation between the

total intensity flux density and the polarization fraction, the number counts $n(P) \equiv \mathrm{d}N/\mathrm{d}P$ can be determined by

$$n(P) = \int_{S_0=P}^{\infty} \mathcal{P}\left(m = \frac{P}{S}\right) n(S) \frac{\mathrm{d}S}{S}, \quad (7)$$

where $n(S)$ is the assumed source counts in total intensity, and $\mathcal{P}$ is the probability density distribution for the polarization fraction m, i.e. $\Pi/100$. Note that in each bin in P, the integration over S is truncated at $S_0 = P$, which corresponds to the maximum degree of the polarization fraction (i.e. $m = 1.0$). We compare our results with source counts provided by Massardi et al. (2013, blue diamonds) via Markov Chain Monte Carlo (MCMC) simulation of the whole AT20G catalogue (Massardi et al. 2011), as well as with the Tucci & Toffolatti model (2012, red and blue lines, which refer to the lower and upper levels expected, respectively). Since our sample is mainly composed by blazars (BL Lacs and FSRQs), which typically are labelled as 'flat' and represent the dominant population at 20 GHz (dashed lines), we expect and find a good agreement with the limits on the total source counts provided by the model. Hence, given the assumptions of Tucci & Toffolatti (2012) on the median polarization fraction of steep-spectrum radio sources (presented in their table 4), which are higher than our current findings (see our Fig. 5, for a comparison), their overestimation of source number counts in polarization below 10 mJy can be (at least partially) explained. Note that equation (7) assumes independence of the polarization fraction from the total flux density. However, this assumption can be broken as another population with different polarization properties, namely steep-spectrum sources, becomes increasingly important with decreasing flux density.

6 CONCLUSIONS

We have presented and discussed high-sensitivity polarimetric observations in seven bands, centred at 2.1, 5.5, 9, 18, 24, 33, and 38 GHz, of a complete sample of 104 extragalactic sources with $S_{20\,\mathrm{GHz}} \geq 200$ mJy in the AT20G catalogue. The rms error in the polarized flux density is 0.6 mJy at $\nu \geq 5.5$ GHz and 1 mJy at 2.1 GHz, due to the heavy RFI contamination.

Polarization measurements in the range 5.5–38 GHz for 53 objects of the sample were reported by Galluzzi et al. (2017). The measurements for the other 51 sources are new, as are the 2.1 GHz measurements for the full sample of 104 sources. The 53 sources were re-observed at 5.5 and 9 GHz, while we managed to repeat the observations at 18, 24, 33, and 38 GHz only for 20 per cent of them. The previous measurements at 33 and 38 GHz were re-calibrated using the updated model for the flux density absolute calibrator, PKS1934−638, that was not available for the earlier analysis.

The observational determination of the continuum spectra has been extended by exploiting the GLEAM survey data at 20 frequencies between 72 and 231 MHz (Hurley-Walker et al. 2017), available for 89 ($\simeq$86 per cent) of our sources. For these sources, we have the unparalleled coverage of 2.7 decades in frequency.

The total intensity data from 5.5 to 38 GHz could be interpreted in terms of a single emission region (Galluzzi et al. 2017). A joint analysis of the more extended total intensity spectra (from 72 MHz to 38 GHz) presented here and of the polarization spectra reveals a more complex astrophysics. About 93 per cent of our sources show clear indications of at least two emission components, one (or sometimes more) dominating at the higher frequencies and self-absorbed at a few GHz, and another one, generally steeper, emerging at lower frequencies. The most straightforward interpretation of these results is in terms of recurrent activity, with the extension (and, correspondingly, the age) of emission components increasing with decreasing frequency, i.e. with younger components showing up at higher frequencies.

There is no evidence of trends of the linear polarization fraction with the frequency for the full sample and for the single component ('1C') subset. However, sources with two or three components ('2–3C') have a minimum of the polarization fraction at $\simeq$ 9 GHz, consistent with different emission components at lower and higher frequencies. For multicomponent ('>3C') objects, there is a hint of a *decrease* with increasing frequency of the polarization fraction, although the statistics are very poor.

Further indications of different origins for the low- and high-frequency emissions come from our analysis of RMs. The data suggest two regimes for the RM versus λ^2 relation, one at cm-wavelengths, with typical *intrinsic* RM of $\sim$90 rad m^{-2}, and the other for mm-wavelengths with median intrinsic RM $\sim$ 2000 rad m^{-2} (but with very large errors). The '>3C' seem to have very high RMs ($\sim$4000 rad m^{-2}). Again, the statistics are very poor but it is suggestive that, at mm-wavelengths, the large RMs echo the low polarization fraction.

Our high sensitivity polarimetry has allowed a 5σ detection of the weak circular polarization for $\sim$38 per cent of data. The measured values of Stokes V, while much lower than the linear polarization amplitude, are much higher than expected for the intrinsic circular polarization of synchrotron emission corresponding to the typical magnetic field intensities in radio emitting regions. This is consistent with previous conclusions in the literature that circular polarization is predominantly produced by Faraday conversion of linear polarization.

Finally, we have presented a new estimate of the counts in linear polarization at 20 GHz derived from the convolution of the distribution of polarization fractions for our sample with the model for total intensity source counts by De Zotti et al. (2005) that, thanks to the high sensitivity of our data, allows us to reach deeper polarized flux density levels than obtained so far.

ACKNOWLEDGEMENTS

We thank the anonymous referee for useful comments. We acknowledge financial support by the Italian *Ministero dell'Istruzione, Università e Ricerca* through the grant *Progetti Premiali 2012-iALMA* (CUP C52I13000140001). Partial support by ASI/INAF Agreement 2014-024-R.1 for the *Planck* LFI Activity of Phase E2 and by ASI through the contract I-022-11-0 LSPE is acknowledged. We thank the staff at the ATCA site, Narrabri (NSW), for the valuable support they provided in running the telescope and in data reduction. The ATCA is part of the Australia Telescope which is funded by the Commonwealth of Australia for operation as a National Facility managed by CSIRO. AB acknowledges support from the European Research Council under the EC FP7 grant number 280127. VG thanks Rocco Lico for the useful discussions. VC acknowledges DustPedia, a collaborative focused research project supported by the European Union under the Seventh Framework Programme (2007–2013) call (proposal no. 606824). The participating institutions are: Cardiff University, UK; National Observatory of Athens, Greece; Ghent University, Belgium; Université Paris Sud, France; National Institute for Astrophysics, Italy, and CEA (Paris), France. LT and LB acknowledge partial financial support from the Spanish Ministry of Economy and Competitiveness (MINECO), under project AYA-2015-65887-P.

REFERENCES

Agudo I., Thum C., Wiesemeyer H., Krichbaum T. P., 2010, ApJS, 189, 1
Agudo I., Thum C., Gómez J. L., Wiesemeyer H., 2014, A&A, 566, A59
Arkin H., Colton R. R., 1970, Statistical Methods, 5th edn. Barnes & Noble, New York
Battye R. A., Browne I. W. A., Peel M. W., Jackson N. J., Dickinson C., 2011, MNRAS, 413, 132
Bonavera L., Massardi M., Bonaldi A., González-Nuevo J., De Zotti G., Ekers R. D., 2011, MNRAS, 416, 559
Callingham J. R. et al., 2015, ApJ, 809, 168
De Zotti G., Ricci R., Mesa D., Silva L., Mazzotta P., Toffolatti L., González-Nuevo J., 2005, A&A, 431, 893
Farnes J. S., Gaensler B. M., Carretti E., 2014, ApJS, 212, 15
Galluzzi V. et al., 2017, MNRAS, 465, 4085
Gehrels N., 1986, ApJ, 303, 336
Hurley-Walker N. et al., 2017, MNRAS, 464, 1146
Johnston-Hollitt M., Ekers R. D., 2004, preprint (astro-ph/0411045)
Massardi M. et al., 2008, MNRAS, 384, 775
Massardi M. et al., 2011, MNRAS, 412, 318
Massardi M. et al., 2013, MNRAS, 436, 2915
Mauch T., Murphy T., Buttery H. J., Curran J., Hunstead R. W., Piestrzynski B., Robertson J. G., Sadler E. M., 2003, MNRAS, 342, 1117
Murphy T. et al., 2010, MNRAS, 402, 2403
Oppermann N. et al., 2015, A&A, 575, A118
Pacholczyk A. G., 1973, MNRAS, 163, 29p
Partridge B., López-Caniego M., Perley R. A., Stevens J., Butler B. J., Rocha G., Walter B., Zacchei A., 2016, ApJ, 821, 61
Pasetto A., Kraus A., Mack K.-H., Bruni G., Carrasco-González C., 2016, A&A, 586, A117
Rayner D. P., Norris R. P., Sault R. J., 2000, MNRAS, 319, 484
Ruszkowski M., Begelman M. C., 2002, ApJ, 573, 485
Sajina A., Partridge B., Evans T., Stefl S., Vechik N., Myers S., Dicker S., Korngut P., 2011, ApJ, 732, 45
Sault R. J., 2003, ATNF Memo, AT/39.3/124
Sault R. J., Teuben P. J., Wright M. C. H., 1995, in Shaw R. A., Payne H. E., Hayes J. J. E., eds, ASP Conf. Ser. Vol. 77, Astronomical Data Analysis Software and Systems IV. Astron. Soc. Pac., San Francisco, p. 433
Tingay S., de Kool M., 2003, ApJ, 126, 723
Tucci M., Toffolatti L., 2012, Adv. Astron., 2012, 624987
Tucci M., Martínez-González E., Toffolatti L., González-Nuevo J., De Zotti G., 2004, MNRAS, 349, 1267
Wardle J. F. C., Homan D. C., 2003, Ap&SS, 288, 143
Wardle J. F. C., Kronberg P. P., 1974, ApJ, 194, 249

SUPPORTING INFORMATION

Supplementary data are available at *MNRAS* online.

Please note: Oxford University Press is not responsible for the content or functionality of any supporting materials supplied by the authors. Any queries (other than missing material) should be directed to the corresponding author for the article.

[1]*INAF, Istituto di Radioastronomia, Via Piero Gobetti 101, I-40129 Bologna, Italy*
[2]*Dipartimento di Fisica e Astronomia, Università di Bologna, via Gobetti 93/2, I-40129 Bologna, Italy*
[3]*Jodrell Bank Centre for Astrophysics School of Physics & Astronomy, The University of Manchester, Manchester M13 9PL, UK*
[4]*INAF - Osservatorio Astrofisico di Arcetri, Largo Enrico Fermi 5, I-50125 Firenze, Italy*
[5]*Dipartimento di Fisica e Scienze della Terra, Università degli Studi di Ferrara, Via Giuseppe Saragat 1, I-44100 Ferrara, Italy*
[6]*INFN-Sezione di Ferrara, Via Giuseppe Saragat 1, I-44122 Ferrara, Italy*
[7]*INFN-Sezione di Bologna, Via Irnerio 46, I-40126 Bologna, Italy*
[8]*INAF, Osservatorio Astronomico di Padova, Vicolo dell'Osservatorio 5, I-35122 Padova, Italy*
[9]*CSIRO Astronomy and Space Science, PO Box 76, Epping, NSW 1710, Australia*
[10]*International Centre for Radio Astronomy Research, Curtin University, Bentley, WA 6102, Australia*
[11]*Departamento de Física Universidad de Oviedo c. Federico García Lorca, 18, E-33007 Oviedo, Spain*
[12]*European Space Agency, ESAC, Camino bajo del Castillo, s/n, Urbanización Villafranca del Castillo, Villanueva de la Cañada, E-28692 Madrid, Spain*
[13]*INAF-IASF Bologna, Via Piero Gobetti 101, I-40129 Bologna, Italy*
[14]*Département de Physique Théorique and Center for Astroparticle Physics (CAP), University of Geneva, 24 quai Ernest Ansermet, CH-1211 Geneva, Switzerland*
[15]*ASTRON, the Netherlands Institute for Radio Astronomy, Postbus 2, NL-7990 AA Dwingeloo, the Netherlands*

This paper has been typeset from a TEX/LATEX file prepared by the author.